X-ray spectroscopy of 1 cm plasma channels produced by self-guided pulse propagation in elongated cluster jets

K. Y. Kim and H. M. Milchberg

Institute for Physical Science and Technology, University of Maryland, College Park, Maryland 20742, USA

A. Ya. Faenov, A. I. Magunov, T. A. Pikuz, and I. Yu. Skobelev

Multicharged Ions Spectra Data Center of VNIIFTRI, Mendeleevo, 141570 Moscow Region, Russia

(Received 30 November 2005; published 16 June 2006)

We diagnose the self-channeled propagation of intense femtosecond pulses over an extended distance in a N_2O cluster gas target using high resolution kilovolt x-ray pinhole images of the channel and spatially resolved x-ray spectra. The x-ray images are consistent with femtosecond optical scattering, shadowgraphy, and interferometry images. We observe extended plasma channels ($\sim$9 mm) limited either by the cluster jet length or by absorption, for injected laser intensities in the range of 10^{16}–10^{17} W/cm^2. Spectral line shapes for the OVII $1s^2$-$1s3p$ and OVIII $1s$-$2p$ transitions (at 1.8627 and 1.8969 nm, respectively) show significant broadening to the blue side and with truncated emission on the red side. We attribute this effect to Doppler blueshifted emission from fast ions from exploding clusters moving toward the spectrometer; redshifted emission from the opposite side of the cluster is absorbed.

PACS number(s): 52.50.Jm, 36.40.Gk, 36.40.Vz

I. INTRODUCTION

One of the outstanding goals in the study of high intensity, ultrashort laser interaction with matter has been the extension of the self-guided interaction length. Such extended high intensity propagation has an application to laser-driven acceleration [1], advanced coherent sources of extreme ultraviolet radiation and x rays [2], and the fast igniter fusion scheme [3]. In plasmas, tightly focused multiterawatt laser beams have been used for this purpose. In those experiments, the main approach has been to increase laser intensity to levels beyond $\sim$10^{18} W/cm^2 in order to promote relativistic self-focusing, followed by whole-beam ponderomotive filamentation [4]. High-pressure gas jet targets, which typically yield subcritical electron density plasmas when ionized by the laser field, have been the most popular media for such intense laser pulse self-guiding. Relativistic self-guiding has been previously demonstrated over no more than $\sim$2 mm, with that length limited by pulse scattering and erosion owing to Raman instabilities and ionization-induced refraction [5]. Here we report the results of another approach, using clustered gas jets, where we observe intense pulse self-channeling over nearly 1 cm, the length of the cluster jet plume. The effect can occur at almost four orders of magnitude less intensity than required for relativistic self-focusing or ponderomotive filamentation. X-ray and optical imaging were used to observe extended laser channeling and to estimate plasma parameters along the resulting plasma channel. We note that in other works, $\sim$0.4 mm long plasma columns were observed in intense 0.7 terawatt ultraviolet laser interactions with Xe cluster jets [6].

We have demonstrated in earlier experiments and calculations that the self-guiding effect is made possible by the optical response presented by the strongly heated clusters as they explode in the presence of the driving laser field [7–9]. In the regime of moderate laser intensities ($\lesssim$10^{16} W/cm^2) and large clusters ($\gtrsim$100 Å), where a hydrodynamic model

of the cluster response is appropriate, the cluster polarizability is positive (refractive index contribution is positive) as long as the dominant optical response of the cluster is from constituent plasma in excess of critical density [7–9]. The onset of positive polarizability occurs faster at the beam center compared to the edge, so that a transient refractive index profile occurs which is well suited for the self-focusing of the beam. We have experimentally demonstrated such self-focusing in short cluster jets under the conditions of moderate intensity and large cluster size [9]. For higher intensities, the hydrodynamic model loses validity because laser-driven electron orbits become comparable to the cluster size. For that regime, we have developed a new particle-in-cell (PIC) model for the cluster response [10]. In that case, the cluster polarizability can be strongly enhanced to large positive values when the intensity reaches a threshold whereby the field-driven electrons transit the cluster in a time equal to the laser period. Although self-focusing would be expected in that case as well, it remains to do a simulation of pulse propagation under these conditions. That will be the subject of future work.

II. EXPERIMENTAL SETUP

In our experiments, 50 mJ, 800 nm pulses at 10 Hz from a Ti:sapphire laser system were focused by a $f/5$ lens into an elongated cluster jet pulsed at 10 Hz with N_2O as the working gas at a valve backing pressure of 400 psi. The experimental setup is shown in Fig. 1. The cluster jet was produced by a high aspect ratio slit nozzle backed by a high-pressure pulsed valve. The nozzle outlet had dimensions 11.5 mm × 0.4 mm, with the laser injected parallel to the long side. The valve body was encased by a copper cooling block which was fed by a liquid nitrogen reservoir. The valve temperature was monitored by a thermocouple and precisely controlled to within 0.2 K via feedback by two resistive heating elements, also encased in the block. The laser propa-
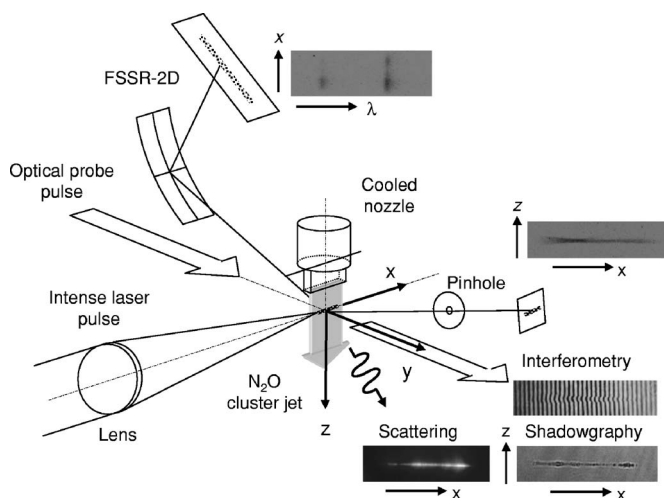
FIG. 1. Experimental setup and typical optical and x-ray images of femtosecond laser-produced N_2O cluster plasmas.

gation axis was 2 mm below the nozzle orifice and the beam was focused 3 mm before the axial midpoint of the nozzle. Compared to our earlier experiments on self-focusing in short 3 mm cluster jets [9], we used significantly more energy (~7 times) here in order to compensate for the strong absorption of the laser pulse by the cluster plasma along the propagation path. N_2O readily forms large clusters even for the gas jets at room temperature and the relatively uncomplicated soft x-ray spectra of highly ionized oxygen ions provide an opportunity for ~1 keV soft x-ray spectroscopic diagnostics of plasma parameters. By contrast, the soft x-ray spectroscopy of ionized argon, used in our earlier experiments [11], is more difficult to interpret for plasma diagnostics purposes. In the experiments, the laser pulse width was adjusted to be either 70 fs (0.7 TW) or 500 fs (0.1 TW). The full width at half maximum (FWHM) of the laser vacuum spot was ~13 μm, corresponding to a Rayleigh length of $z_0 \sim 480$ μm. At the vacuum beam waist, the pulse peak intensity was ~2.5×10^{17} W/cm^2 for the 70 fs pulse and ~3.5×10^{16} W/cm^2 for the 500 fs pulse. Under our valve operating conditions, we estimated average cluster radii of 350 Å for the case of valve cooling to −40 °C and 200 Å for the valve at room temperature. These results were obtained by scaling our previous measured results for argon clusters [12] using the same elongated jet under the same pressure and temperature operating conditions by assuming that N_2O has a similar Hagena k value [13] as Xe and the same packing geometry.

Optical and x-ray imaging methods were used in our experiments to verify the occurrence of extended propagation in the cluster jet. The optical diagnostics used were femtosecond time-resolved interferometry and shadowgraphy, and the imaging of 90° Rayleigh scattering of the propagating laser pulse. The interferometry and/or shadowgraphy probe pulse propagated orthogonally to the generated plasma channel, crossing it ~10 ps after the pump pulse exited the far end of the gas jet. A filtered x-ray pinhole camera obtained images of the plasma channel at photon energy >0.6 keV (using a 2 μm thick polypropylene filter coated with 0.4 μm of Al). A high luminosity, large aperture imaging spectrom-

eter [14] with a spherically bent ($R=150$ mm) mica crystal was used for measurements of soft x-ray spectra in the wavelength range 18.5–19.1 Å, spatially resolved along the laser propagation direction with axial resolution ~40 μm. Spatially resolved spectra of the He-β $1s3p$-$1s^2$ emission of He-like oxygen (OVII) (1.8627 nm) and the Ly-α $2p$-$1s$ emission of H-like oxygen (OVIII) (1.8969 nm) were obtained with spectral resolution $\Delta\lambda/\lambda \sim 5000$. The x-ray images were recorded on KODAK RAR 2492 films using approximately 20 000 shots.

III. SIMULATIONS OF LASER-HEATED CLUSTER EVOLUTION

The laser-cluster interaction is simulated self-consistently by coupling the equation for the electric near field, $\nabla \cdot (\varepsilon \mathbf{E}) = 0$, to a one-dimensional (1D) radial Lagrangian hydrocode Full details of the hydrocode can be found in Ref. [7]. The near field treatment is appropriate for the case where $ka \ll 1$, where k is the laser wave number and a is the maximum radius of the expanding cluster plasma. This is a good approximation for initial cluster sizes much smaller than a laser wavelength and for times not too late in the cluster expansion. The dielectric function of the cluster material is taken to be of Drude form $\varepsilon(r) = 1 + 4\pi N_0 \alpha (1 - N_0 \alpha/3)^{-1} - \xi + i\xi \nu/\omega$. Here $N_0(r)$ is the density of neutral atoms, α is the atomic polarizability, and $\xi(r) = [1 + \nu^2(r)/\omega^2]^{-1} N_e(r)/N_{cr}$, where $N_e(r)$ is the electron density, ω is the laser frequency, and $\nu(r)$ is the collision frequency. The latter is obtained by summing the rates of electron collision with each of the neutral and ion species. The calculation includes tunneling ionization by the laser field, collisional ionization, and both collisional-radiative (CR) and local thermal equilibrium (LTE) models for the ionization dynamics. The CR model can be run in either a time-dependent mode or a steady state mode. In general, we find that results from the steady state CR and LTE models converge at the highest densities in the cluster core. For 100 fs pump pulses, however, the time-dependent CR model gives different results, even at the highest densities. Therefore, the time-dependent CR model is used in the simulations of this paper.

Starting with a solid density neutral cluster, at each time step the equation for the electric near field is solved using the neutral, ion, and electron density profiles and the temperature profile of the previous time step, and the resulting electric field ionizes and heats the plasma, driving the cluster dynamics. Thermal conduction at each Lagrangian gridpoint is taken to be the lesser of the gradient-based value $|\kappa \partial T_e/\partial r|$, where κ is the thermal conductivity and T_e is the electron temperature, and the flux-limited flow. An ideal gas equation of state is used for the cluster plasma. While this is a reasonable assumption at the high temperatures generated by the laser interaction, it cannot take into account any hot electrons generated in the interaction, which are decoupled from the thermal distribution. A more accurate treatment using our PIC code [10] is appropriate for cases where the hot electron population is a significant fraction of the total, which could be the case for smaller clusters. The model is best suited to intensity levels $\lesssim 10^{16}$ W/cm^2, where the size of laser-driven

electron orbits is smaller than typical large cluster radii of a few hundred Å. For higher intensities one must use the PIC simulation [10] or a molecular dynamics simulation [15]. Our PIC simulations have shown that the fraction of electrons is quite small which contribute to a laser-driven halo of electrons with orbits exceeding the cluster size. In terms of understanding the soft x-ray emission measured in this experiment, the evolution of the bulk plasma electron density and temperature are important. While the coupling of the hot laser-driven halo electrons to the bulk plasma is not accounted for by the hydrocode, we note that the intensity used in the simulations shown here produces a level of ionization consistent with the measured spectra in Sec. IV. For this reason we use the hydrocode to provide physical insight into the plasma dynamics leading to the observed x-ray emission.

Because the hydrocode can simulate only single-species clusters, as a stand-in for N_2O we consider nitrogen clusters. Nitrogen ions are sufficiently close in mass and electronic structure to oxygen ions that our results for density and temperature evolution should be sufficient to provide reasonable physical insight. For the simulation parameters, we took a peak intensity of 3×10^{16} W/cm^2, laser wavelength 800 nm, Gaussian laser pulsewidth 100 fs, cluster radius 350 Å, and intracluster density 2×10^{22} atoms/cm^3. The peak intensity is somewhat beyond the limit of the applicability of the code, but it is sufficient to produce a maximum ionization state midway between hydrogenic and fully stripped nitrogen in accord with the experimental observation of spectrally dominant emission from hydrogenlike and heliumlike oxygen ions. Full details of the code are given in Ref. [7].

Figure 2(a) plots the electron temperature T_e and ion temperature T_i, with the laser pulse envelope overlaid on the plot as a reference. Figure 2(b) shows the electron density N_e at the center of the cluster plasma as a function of time, also overlaid with the laser pulse envelope. It is seen that after laser heating to an electron temperature of almost 1 keV and peak electron density in excess of 10^{23} cm^{-3}, the electron temperature and density drop by rough factors of 100 and 1000, respectively, in less than 1 ps. Note that because the cluster is small and the thermal conductivity is high, the temperature profile vs plasma radius is almost flat. It is seen that the ions are not in equilibrium with the electrons for the full simulation, with $T_e > T_i$ at early times, and $T_i > T_e$ at later times. Figure 2(c) shows the mass-weighted average degree of ionization Z in the plasma as a function of time, again overlapped with the laser pulse envelope as a reference. An initial rapid rise in ionization is coincident with the intensity passing through the threshold for optical field ionization of neutral nitrogen near $\sim 10^{14}$ W/cm^2 [16]. The ionization level then rises more slowly as the collisional ionization driven by laser thermal heating takes over and peaks in the range $Z \sim 6-7$. This corresponds to dominant populations of H-like and fully stripped nitrogen. After the maximum electron density is achieved and the expansion is well underway [see Fig. 2(b)], Z slowly declines to ~ 6.4 by the end of the simulation at 2 ps.

For the interpretation of measurements of time-integrated Ly-α and He-β line spectra shown in Sec. IV below, it is useful to consider the temporal origin of the line emission, for which the simulation provides physical insight. From the
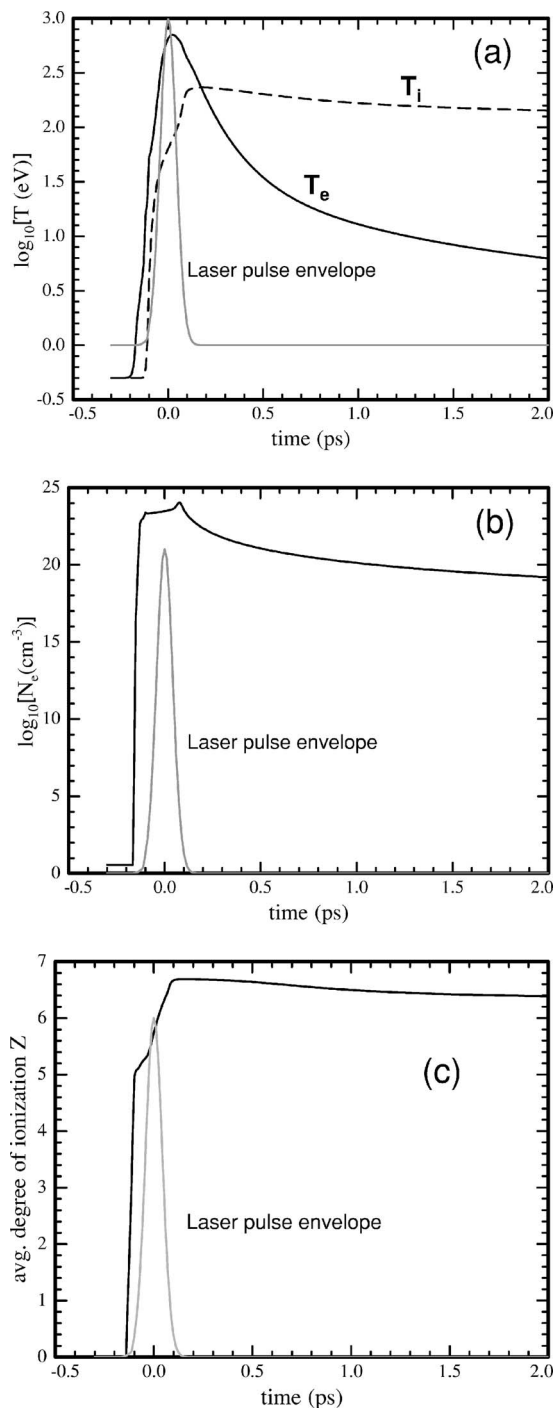

FIG. 2. Self-consistent hydrocode simulation of 3×10^{16} W/cm^2, 100 fs, $\lambda = 800$ nm pulse interacting with a 350 Å radius nitrogen cluster. (a) Plot of the cluster central electron and ion temperatures vs time, overlaid with laser pulse envelopes. (b) Cluster central electron density vs time. (c) Mass-weighted average degree of ionization Z vs time.

evolution of Z seen in Fig. 2(c), it may be expected that the spectra have contributions from two phases. The first phase is the prompt line emission during laser heating of the cluster plasma, with strong electron collisional excitation from the dominant ion ground states occurring at high plasma density and temperature. As the laser pulse turns off, this emission

can continue as long as the plasma is sufficiently hot and dense. In the second phase, the cluster rapidly expands and cools, and the temperature becomes too low for collisional excitation of line emission. However, the persistence of $Z \sim 6-7$ well past the laser pulse guarantees a reservoir of ions into which three-body recombination of electrons feeds a cascade through upper bound states, ultimately resulting in photon emission from strongly bound state transitions such as Ly-α and Ly-β ($2p$-$1s$ and $3p$-$1s$ in the H-like ion) and He-α and He-β ($1s2p$-$1s^2$ and $1s3p$-$1s^2$ in the He-like ion). The reservoir of high ion stages persists because the cooling rate is much faster than the recombination rate.

As a qualitative measure of the relative contribution of the two phases to Ly-α emission in H-like nitrogen (N^{6+}), Fig. 3(a) plots the cluster volume-integrated $1s$-$2p$ electron collisional excitation rate of the ground state of N^{6+}, $R_{12}(t) = \int_0^{R(t)} dr\, 4\pi r^2 N_e(r,t) N_6(r,t) S_{12}(T_e(r,t))$, and the three-body recombination rate from fully stripped nitrogen (N^{7+}) to high bound states of N^{6+}, $R_{3b}(t) = \int_0^{R(t)} dr\, 4\pi r^2 N_e^2(r,t) N_7(r,t) \alpha_{3b}(T_e(r,t))$. Each of these processes feeds Ly-α ($2p$-$1s$) emission in N^{6+}. Here $R(t)$ is the radius of the expanding cluster containing 100% of its mass, N_e is the electron density, N_6 and N_7 are the densities (cm^{-3}) of N^{6+} and N^{7+}, T_e is the electron temperature, S_{12} (cm^3 s^{-1}) is the electron collisional excitation rate, and α_{3b} (cm^6 s^{-1}) is the three-body recombination rate. For reference, overlaid on the plot is the laser pulse envelope. It is seen that collisional excitation of Ly$_\alpha$ rises and falls closely coincident with the laser pulse, but the contribution of recombination comes later and even extends beyond the end of the simulation at 2 ps. The time integral of R_{3b} is $\sim 20\%$ greater than that of R_{12}. This comparison still underestimates the relative contribution of recombination because at the high density and temperatures at early times, collisional deexcitation reduces the $2p$ population more than it would at the low densities and temperatures of the recombination phase.

Our conclusion is that the recombination cascade contributes significantly to the measured time-integrated line spectra from H-like and He-like oxygen lines in N_2O cluster plasmas. Plasma conditions during rapid cluster expansion should therefore play a role in determining details of the spectral line shape. For a later consideration of Doppler shifts, Fig. 3(b) shows velocity profiles for cluster plasma flows at several times in the cluster explosion. An estimate of the effective cluster size as a function of time is shown in Fig. 3(c), which plots the time-dependent radii $R_{1/2}(t)$ and $R_{full}(t)$ within which 50% and 100% of the expanding cluster mass is contained. The plasma velocity profile and effective size will be used in Sec. IV for calculations of absorption of line emission.

IV. EXPERIMENTAL RESULTS AND DISCUSSION

We examined the laser pulse interaction with the uncooled N_2O cluster jet under a long pulse [500 fs, Fig. 4(a)] and short pulse [70 fs, Fig. 4(b)] irradiation. Extended channels up to ~ 9 mm in length are shown by the optical and x-ray images. The channels generated with the 70 fs pulse are
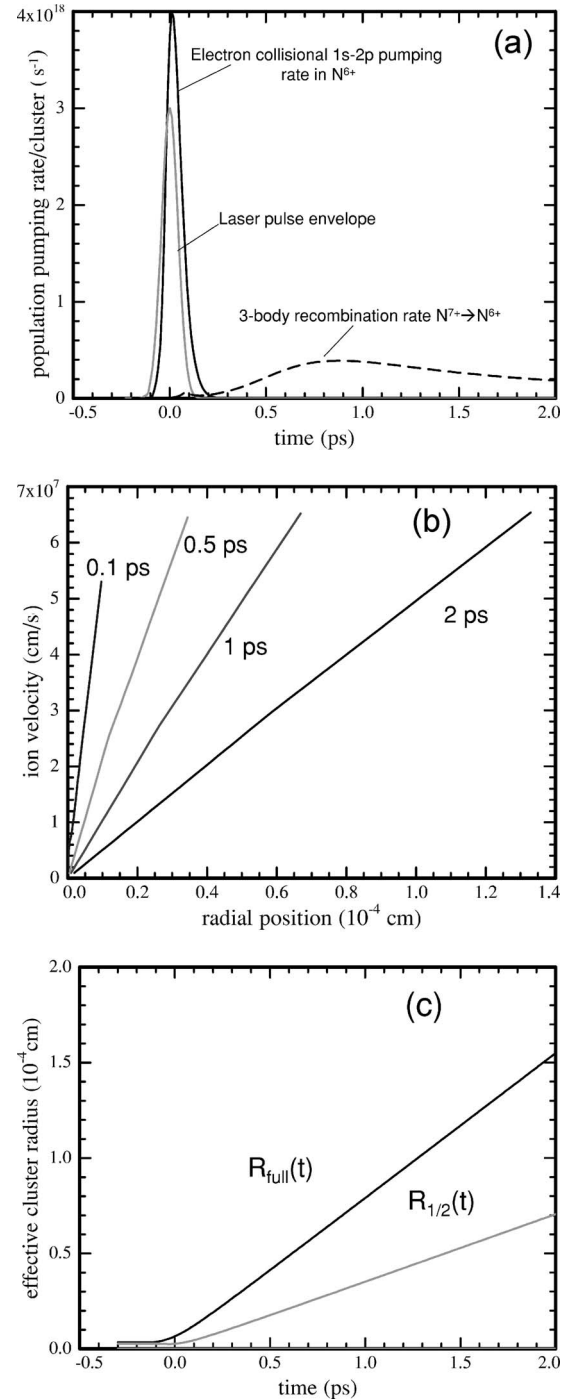

FIG. 3. For conditions of Fig. 2: (a) Electron collisional $1s$-$2p$ pumping rate in N^{6+} and three-body recombination rate $N^{7+} \rightarrow N^{6+}$. (b) Ion velocity profiles at selected times ($t=0$ is the peak of the laser pulse). (c) Radial position of expanding spherical surfaces containing 50% of the cluster mass ($R_{1/2}$) and 100% of the cluster mass (R_{full}).

slightly shorter than those generated with the 500 fs pulse. The images show plasmas of constant diameter for distances well beyond the Rayleigh range (~ 0.5 mm) of the vacuum beam, with the pulse propagating to the end of the jet. For both the 500 and 70 fs pulses, the diameter of the >0.6 keV x-ray emission zone is ~ 100 μm, and this extends for the
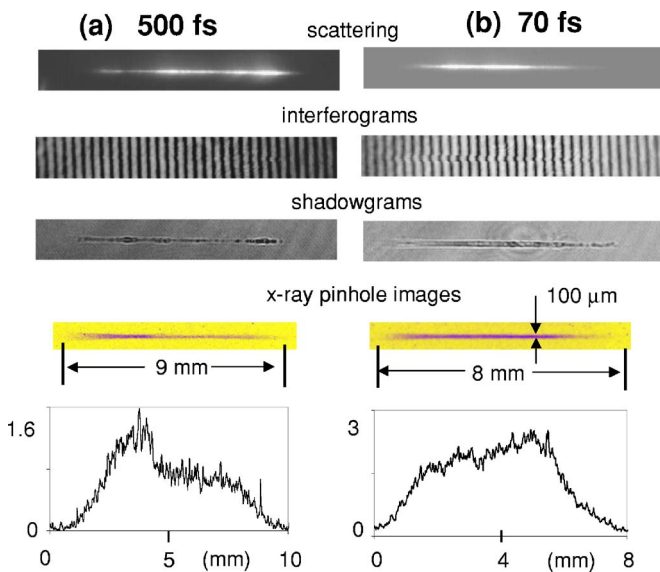
FIG. 4. (Color online) Rayleigh scattering images, interferograms, shadowgrams, x-ray pin-hole images, and axial pin-hole image lineouts of laser-produced N_2O cluster plasmas for laser pulse durations of (a) 500 fs and (b) 70 fs. The laser vacuum focus is located at 3 mm before the center of the elongated N_2O cluster jet at a 400 psi gas jet backing pressure and room temperature. The laser pulse enters from the left.

full length of propagation. Axial lineouts are shown below their corresponding x-ray pinhole images. The interferograms show relatively uniform axial electron densities along the propagation length with average values of $N_e=1.5 \times 10^{18}$ cm^{-3} and 3×10^{18} cm^{-3} for the 500 and 70 fs pulse cases, respectively. As the probe pulse crosses the plasma $\sim$20 ps after the clusters midway along the pump propagation path have exploded, these densities occur after the cluster plasmas have expanded and merged.

When the cluster size is increased by cooling the gas jet valve to $-40\,°C$, the propagation length shortens for both 500 and 70 fs pulses, as seen in Fig. 5, and the average electron density increases to $N_e=10^{19}$ cm^{-3} and 2×10^{19} cm^{-3}, respectively. The optical images and the x-ray images for this case show a much stronger taper than in Fig. 2 owing to the greater rate of absorption along the propagation direction. The $>$0.6 keV x-ray emission is approximately 5 times brighter in the case of the cooled jet. The shorter propagation, greater taper, and greater heating is consistent with stronger absorption by larger clusters [7,8]. Note that the extended propagation is strongly dependent on the presence of the cluster plasma. With N_2 as the working gas, our uncooled jet produces no clusters, as verified by Rayleigh scattering measurements [12]. Figure 6 compares shadowgrams for pulse propagation in the unclustered N_2 and clustered N_2O jets, both at room temperature. The clustered gas jet shows a significantly extended propagation distance, even in the presence of a much greater absorption.

Figure 7(a) shows x-ray line spectra results from He-like (He-β $1s3p$-$1s^2$ in OVII ions) and H-like oxygen (Ly-α $2p$-$1s$ in OVIII ions), for the conditions of Fig. 4(a) (500 fs pulse, uncooled jet), axially resolved along the channel
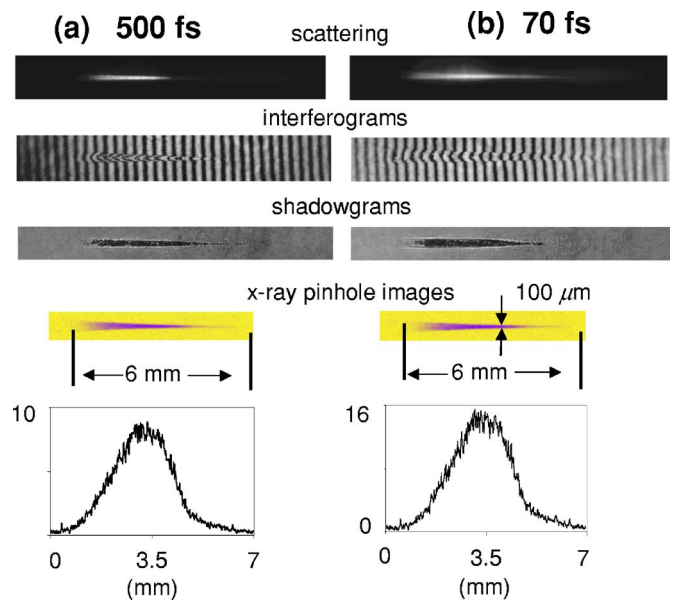

FIG. 5. (Color online) The same as Fig. 4 except that the cluster jet valve is cooled to a temperature $-40\,°C$.

length. A striking feature of both the Ly-α and He-β line shapes is the very pronounced broadening to shorter wavelengths about line center along with a truncation of emission at longer wavelengths. We will discuss this observation later in this section. Axial lineouts of these emissions are shown in Fig. 7(b), while Fig. 7(c) shows a cut along the spectral axis, along with exponential line shape fits.

The axial space distribution of H-like and He-like emission [Fig. 7(b)] is similar to the $>$0.6 keV broadband x-ray pinhole image shown in Fig. 4(a). The ratio of the He-β line to the Ly-α line enables a rough estimation of the bulk time and radial average electron temperature along the channel [17] which is shown in Fig. 7(d). This estimate was obtained from the calculation of the oxygen ion level populations in the collisional-radiative kinetic model by performing a fit to the observed line ratio. The result is based on the stationary solution of rate equations that include all collisional and recombination rates and radiative relaxation [17]. Although the use of time-integrated line ratios gives a "temperature" result which is averaged in an unknown way over time and plasma radius, and over the excitation and recombination phases of the plasma, the result does give a qualitative measure of how plasma parameters vary along the channel axis. As the H-like and He-like oxygen ions have comparable ionization potentials (870 and 740 eV, respectively), one would expect that
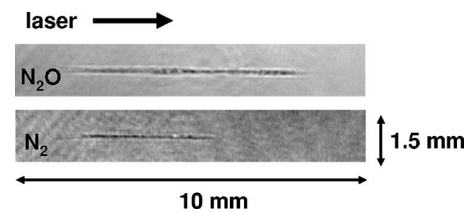

FIG. 6. Shadowgrams for N_2 (nonclustered) and N_2O (clustered) targets at room temperature and 400 psi gas jet backing pressure.
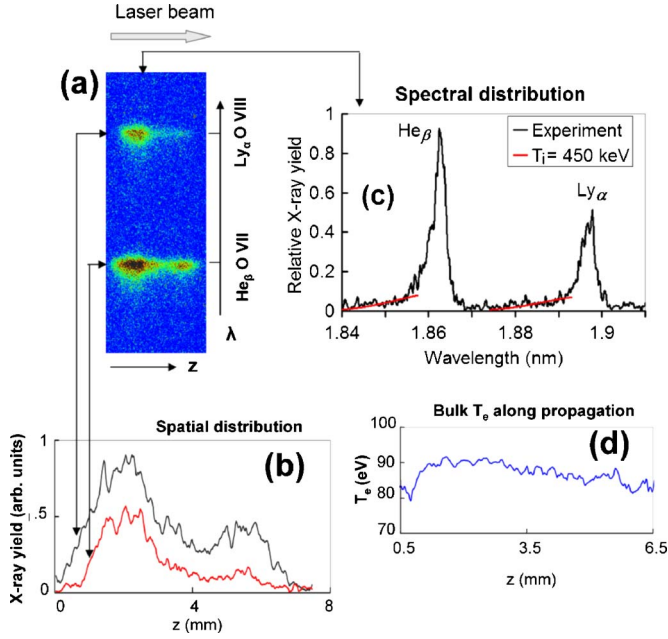
FIG. 7. (Color online) (a) Spatially resolved x-ray line spectra of He-like (He-β $1s^2$-$1s3p$) and H-like oxygen (Ly-α, $1s$-$2p$) from N_2O cluster plasmas under the irradiation of 500 fs, 50 mJ laser pulses with the elongated jet operating at room temperature. (b) Axial lineouts of He-β and Ly-α emissions. (c) Measured line shapes for Ly-α and He-β lines of oxygen ions with a Maxwellian fit to the blue wings. (d) Bulk electron temperature along the channel determined from the intensity ratio of He-β to Ly-α lines.

their respective Ly-α and He-β emissions, whether from excitation or recombination, are strongly linked temporally. That is, plasma conditions that would favor, say excitation of He-like 3-1 emission would not simultaneously strongly favor 2-1 emission in the H-like ion driven by a recombination. Those plasma conditions would favor excitation of the H-like ion. Likewise for recombination: rapid cooling sufficient to drive recombination would likely do so for both ion species simultaneously. The high temperatures, high density, and small radius of the cluster plasma column would give relatively flat temperature profiles, and the mixing of individual cluster explosions into a larger plasma would give relatively flat density profiles. Thus the conditions generating a line ratio in He-like and H-like emissions will be slowly varying across the plasma radius.

Where the laser enters the jet, the line ratio is high, indicating a lower average temperature. After $\sim$1 mm, the ratio drops and then slowly increases for the remainder of the $\sim$8 mm of propagation, indicating a weakly decreasing average temperature. As seen with reference to the simulation in Fig. 2(a), the average temperature 80–90 eV is more representative of the expanding plasma evolution after laser pulse irradiation. Together with the constant electron density along the propagation path, this roughly constant temperature is consistent with relatively uniform and extended propagation. Evidence that the guided laser intensity is high is seen from the high resolution spectral distribution and exponential fits in Fig. 7(c). The pronounced broadening to the blue or short wavelength side indicates the presence of fast

ions with a characteristic average energy $T_{i,fast} \sim 450$ keV (from the fit shown by the red curve). By comparison, in recent experiments using CO_2 clusters [18], fast ions up to 1 MeV were reached only using intensities greater than 10^{18} W/cm^2. Here, for 500 fs pulses, the peak vacuum intensity was 5×10^{16} W/cm^2, a factor of 20 lower.

The asymmetric line shapes of Fig. 7 can be understood as developing from a combination of Doppler broadening and absorption. First it must be determined whether the dominant attenuation comes from the cluster local to the line emission or from the propagation of this emission across the whole gas of exploding clusters. To assess this, we evaluate the ratio τ_{cl}/τ_{gas}, where $\tau_{cl} \sim N_a \sigma a$ and $\tau_{gas} \sim N_{cl}\sigma_{cl}L$. In the first expression, τ_{cl} is the optical depth for intracluster absorption, N_a is the average atomic and/or ionic density internal to the cluster, σ is the effective absorption cross section for a typical ion (from a combination of photoionization, resonant self-absorption, and inverse bremsstrahlung absorption), and a is the radius of the expanding cluster. In the second expression, τ_{gas} is the optical depth for absorption across a distance L of the gas of exploding clusters, N_{cl} is the density of clusters, and σ_{cl} is the effective absorption cross section for a whole cluster. Assuming that absorption in the soft x-ray range is local to atoms and ions within a cluster and does not show a significant whole-cluster effect, we write $\sigma_{cl} = 4\pi N_a a^3 \sigma/3$. Also, we note that $n_{gas} = N_{cl} 4\pi N_a a^3/3 = N_e/Z$ is the average density of atoms and/or ions achieved after the cluster plasmas in the gas expand and merge. Combining these equations using our above measurement of $N_e = 2 \times 10^{19}$ cm^{-3} and $Z \sim 7$ from our spectra and simulations gives $\tau_{cl}/\tau_{gas} \sim 3 \times 10^{-19} N_a a/L$, where N_a is in units of cm^{-3}. During the laser pulse, $a \sim 350$ Å, $N_a \sim 2 \times 10^{22}$ cm^{-3}, and the radial extent of the heated cluster gas is $L \sim w_0 \sim 15$ μm, giving $\tau_{cl}/\tau_{gas} \sim 12$. After 1 ps, $a \sim 1$ μm, L is unchanged and $N_a = 10^{20}$ cm^{-3}, giving $\tau_{cl}/\tau_{gas} \sim 2$. For the cases with lower measured values of N_e discussed above, the values of τ_{cl}/τ_{gas} are even greater. Therefore, under the conditions of our experiments, any affect on line shapes owing to absorption can be dominantly attributed to intracluster absorption of the emitted lines. At longer times in the cluster explosion ($>$1 ps), the contribution of absorption across the macroscopic plasma becomes important.

The absorption mechanisms potentially contributing to the line-shape asymmetry are free-free absorption (inverse bremsstrahlung), bound-free absorption (photo-ionization of neutrals and lower ionization stages), and resonant bound-bound self-absorption (dominantly photoexcitation of low lying bound states from the ground state of the most plentiful ions). The cross sections in cm^2 for these processes are, respectively, $\sigma_{ff} \sim 1.3 \times 10^{-25} \lambda^3 Z^2 N_e/(kT_e)^{1/2}$ [18,19], $\sigma_{bf} \sim 5.5 \times 10^{-17} (\chi/h\nu)^{7/2}/Z^2$ [18,19], and $\sigma_{bb} \sim (g_2/g_1)\lambda^4/(8\pi c t_{sp}\Delta\lambda)$ [20], where λ ($\sim$1.8 nm) is the wavelength of absorbed radiation and $h\nu$ is its photon energy (eV), Z is the degree of ionization, N_e is the electron density (cm^{-3}), kT_e is the electron temperature (eV), χ is the ionization potential (eV), $\Delta\lambda$ is the linewidth (cm), t_{sp} is the spontaneous lifetime (s), and g_2/g_1 is the ratio of statistical weights of the upper and lower bound levels ($g_2/g_1=3$ for the $1s$-$2p$ transition). To determine which of these processes
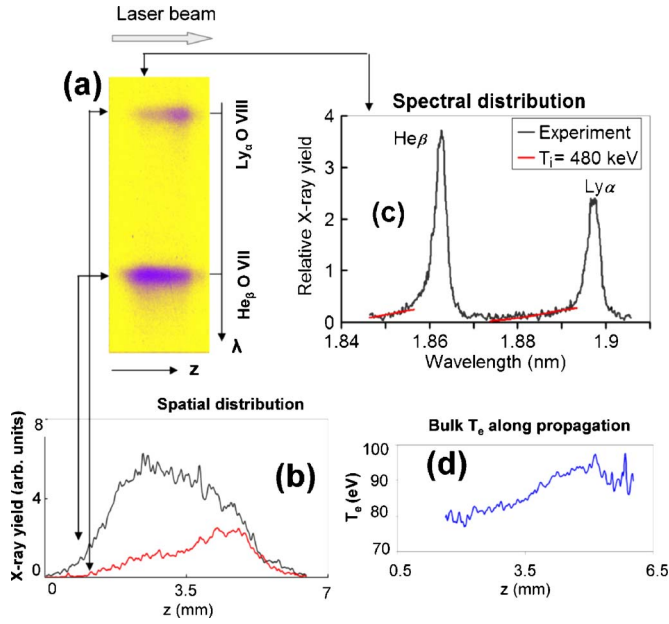
FIG. 8. (Color online) Same as Fig. 7 except that the cluster jet valve temperature is $-30\,°C$.

FIG. 9. (Color online) Dependences of He-β and Ly-α line intensities along the plasma channel on the laser pulse duration. Insets are the space-dependent spectra from which the lineouts were made.

affects the absorption, the cross sections are first compared under conditions which individually maximize them. For inverse bremsstrahlung, we get $\sigma_{ff} \sim 2 \times 10^{-22}$ cm^2 using early time conditions $N_e \sim 10^{23}$ cm^{-3}, $kT_e = 500$ eV, and $Z=7$. For bound-free transitions, $\sigma_{bf} \sim 2.2 \times 10^{-18}$ cm^2 for the peak cross section at threshold, $h\nu = \chi$, and $Z=5$ (ionization profiles from the simulation show $Z>5$ near the edge of the cluster for $0<t<2$ ps). In the expanded lower density plasma regions where the Doppler broadening dominates collisional and Stark broadening, for the $1s$-$2p$ resonant photoexcitation of the OVIII Ly-α line we estimate $\sigma_{bb} \sim 4.1 \times 10^{-16}$ cm^2, using $t_{sp} = 0.3 \times 10^{-12}$ s [21] and $\Delta\lambda/\lambda = 2(2 \ln 2kT_i/mc^2)^{1/2} \sim 1.9 \times 10^{-4}$ for the Doppler broadened linewidth for an ion temperature $kT_i \sim 100$ eV. According to the Griem formula [22] the Stark width for the shifted line components is $\Delta\lambda_S/\lambda \approx 7 \times 10^{-11} n^2 \lambda N_a^{2/3} \sim 3 \times 10^{-2}$, using $N_a = 2 \times 10^{22}$ cm^{-3}. The collisional width for the non-shifted component is $\Delta\lambda_c/\lambda \approx 5 \times 10^{-20} n^4 \lambda N_e / T_e^{1/2} (\ln r_D/r_W + 0.215) \sim 3 \times 10^{-3}$, where the ratio of the Debye radius to the Weisskopf radius is $r_D/r_W \approx 2 \times 10^{11} n^{-2} T_e N_e^{-1/2} \sim 80$. So in the near-solid density region of the cluster at early times in the expansion, the collisional linewidth dominates the Doppler linewidth and σ_{bb} at the line center is reduced to $\sim 3 \times 10^{-17}$ cm^2. While σ_{bb} at the line center is greater than σ_{bf} in all regions of the plasma, σ_{bb} in the wings of the Ly-α line is comparable to σ_{bf} at the high densities at early times. Figure 2(a) shows that $kT_i \sim 100$ eV at both early times during the laser pulse and later in the expansion. The spectral line shape is strongly affected by emission later in the expansion as borne out by the size of the blue wing: the peak expansion velocity of $\sim 10^8$ cm/s shown in Fig. 3(b) develops only after several hundred femtoseconds of cluster expansion and is equivalent to an ion energy of ~ 100 keV. This fluid model result is still significantly less than $T_{i,fast} \sim 450$ keV obtained from the blue wing fit of Fig. 7.
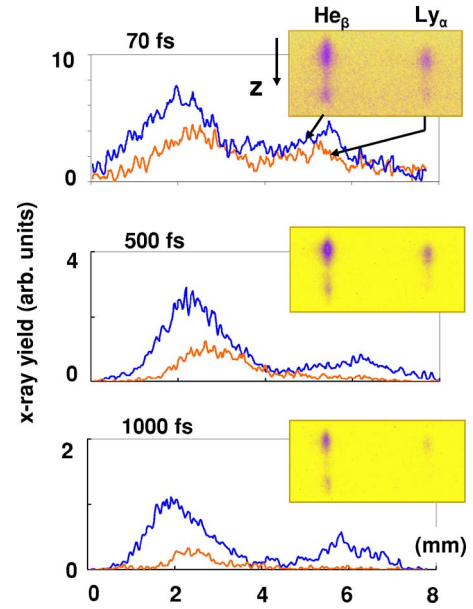
To complete the analysis of these absorption mechanisms we next consider their optical depth τ and the times during which emission occurs. Under the full range of conditions shown in the simulations, τ_{ff} is negligible compared to τ_{bb} and τ_{bf}. The bound-bound and bound-free optical depths are $\tau_{bb} = N_{i-bb} \sigma_{bb} L_{bb}$ and $\tau_{bf} = N_{i-bf} \sigma_{bf} L_{bf}$, where N_{i-bb} and N_{i-bf} are the densities of absorber ions available for each process, $L_{bb} \sim \min\{a, c(dv/dr)^{-1} \Delta\lambda/\lambda\}$ is the effective length over which resonant bound-bound absorption can occur in the presence of the strong velocity gradient of the expanding cluster of radial extent a, and L_{bf} is the full cluster plasma radius, over which nonresonant bound-free absorption can occur. If we consider emission and absorption at early times ($t \sim 50$ fs) near the laser pulse, then $N_{i-bb} \sim N_{i-bf} \sim 10^{22}$ cm^{-3}. For a cluster plasma of size $a \sim 500$ Å from Fig. 3(c), we use $L_{bf} = a$. The values $\Delta\lambda/\lambda \approx \Delta\lambda_c/\lambda \sim 2 \times 10^{-3}$ and $dv/dr \sim 4 \times 10^{11}$ s^{-1} [from Fig. 3(b)] give $L_{bb} \sim \min\{500$ Å$, 1.5 \times 10^{-4}$ cm$\} = 500$ Å. Then $\tau_{bf} \sim 0.1$, $\tau_{bb} \sim 2.1$ at the line center and $\tau_{bb} \sim 0.2$ in the far wings. Therefore, for the line emission driven by the electron collisional excitation at early times in the cluster evolution, resonant self-absorption at line center dominates, but in the line wings it is comparable to bound-free absorption.

At later times $t \sim 0.5$ ps, during the recombination-fed line emission [see Fig. 3(a)], we use $N_{i-bb} \sim N_{i-bf} \sim 4 \times 10^{20}$ cm^{-3}, $N_e \sim 3 \times 10^{21}$ cm^{-3} (for $Z=7$), $L_{bf} = a \sim 0.4 \times 10^{-4}$ cm, $dv/dr \sim 10^{12}$ s^{-1}, Doppler broadening of $\Delta\lambda/\lambda \sim 1.9 \times 10^{-4}$, $\sigma_{bb} \sim 4.1 \times 10^{-16}$ cm^2, and $L_{bb} \sim \min\{0.5 \times 10^{-4}$ cm$, 5.7 \times 10^{-6}$ cm$\} = 5.7 \times 10^{-6}$ cm to get $\tau_{bb} \sim 1$ at the line center (and ~ 0.1 in the wings) and $\tau_{bf} \sim 0.03$. By $t \sim 1$ ps, the density has rapidly dropped to $N_{i-bb} \sim N_{i-bf} \sim 2 \times 10^{19}$ cm^{-3}, giving $\tau_{bb} \sim 0.1$ at the line center and $\tau_{bf} \sim 0.003$.

The above estimates allow a qualitative explanation of the observed line shapes. First, the line emission from the side of
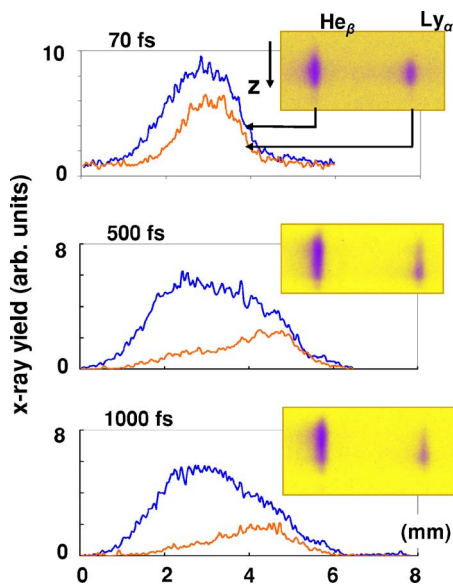
FIG. 10. (Color online) Same as Fig. 9 except that the cluster jet valve temperature is −30 °C.

the exploding cluster farthest from the spectrometer is red-shifted. To reach the spectrometer, this light must propagate back through the cluster and is thus absorbed more strongly than the blueshifted emission from the side of the cluster closest to the spectrometer. For the collisional excitation-driven line emission at early times ($t < 100$ fs, say), $\tau_{bb} \sim 2$ ensures strong resonant self-absorption near the line center on the red side. In the far line wings, bound-bound and bound-free mechanisms contribute comparably, with weaker absorption. Meanwhile, the blue wings are produced from the outer layer of plasma expanding from the cluster toward the spectrometer. At intermediate times (100 fs $< t < 0.5$ ps), $\tau_{bb} > \sim 1$ ensures continued line asymmetry, with a preferential absorption of the red wings. In this phase the nature of the line emission changes from collision-driven to recombination-driven. At later times $t > 1$ ps, there is little absorption of red or blue wings. The net result is a spectrum dominantly broadened to the blue. There is a red wing of limited extent, with the amplitude quickly dropping below the spectrum noise. As the expansion velocity of the cluster outer layers is largest at long times when absorption is small, the blueshifted wings are useful for estimates of fast ion kinetic energy, as has been done in Fig. 7(c).

Note that the above estimates are based on considering clusters of a single size, which determines the specific timescales discussed. In reality the cluster size distribution can be quite wide, with significantly varying timescales from cluster to cluster. However, the general process should still hold: the red spectral wings should be relatively suppressed in favor of the blue wings, and the blue wings should be characteristic of fast ion expansion. Because line absorption is negligible when ions have reached their maximum speeds, fits to the blue wings indicate the fast ion kinetic energy.

Figure 8 shows the same arrangement of data as Fig. 7, except that now the gas jet valve is cooled to −30 °C, providing a bigger average cluster size. In this case, the ratio of Ly-α to He-β emission lines increases [see Figs. 8(a) and
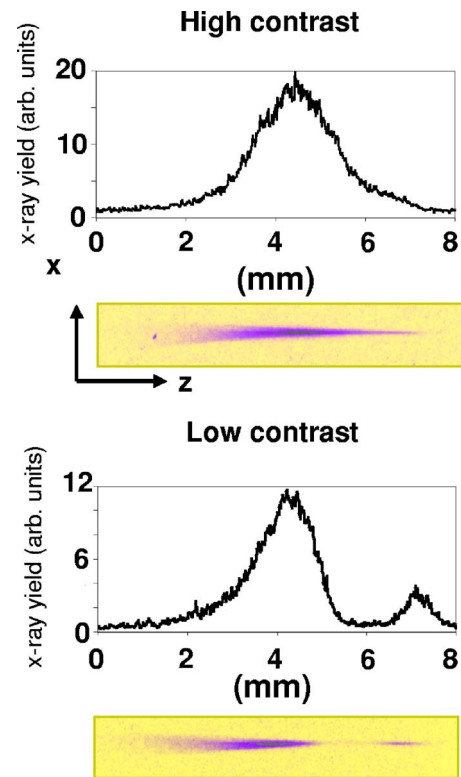

FIG. 11. (Color online) X-ray pinhole images (and their central lineouts) with and without intentional laser prepulses.

8(b)], implying that the laser intensity grows along the propagation direction. This implies that the bulk temperature increases as the laser propagates in the cluster gas [see Fig. 8(d)]. Note that the total x-ray yield is higher for the cooled nozzle, confirming an increase in the average cluster size. The fit of the blue wings in Fig. 8(c) gives the average fast ion energy $T_{i,fast} \sim 480$ keV.

Shown in Fig. 9 is 1D space resolved Ly-α and He-β spectra as a function of pulse duration for the room temperature jet case. From the axial variation of the Ly-α to He-β ratio versus pulse duration, it is seen that average temperatures along the propagation direction drop more rapidly for the longer pulsewidth. As well, the overall yield of x-ray emission drops rapidly with increasing pulsewidth. Figure 10 has the same experimental conditions as Fig. 9 except that the jet valve is cooled. Here, the axial x-ray profiles are more uniform, and they are approximately 2–5 times more intense than that of uncooled case. A striking feature is that the contribution of H-like Ly-α emission increases, while the He-β emission drops, which implies that temperatures increase along the propagation path. The 500 fs pulse gives the most extended and increasing zone of Ly-α emission. The 70 fs pulse gives the shortest emission region up to ~ 4 mm, a distance comparable to the first hump in the uncooled jet x-ray lineouts.

A question arises as to the cause of the double humped x-ray emission in Figs. 7 and 9. A possible origin for the dip in x-ray emission is laser prepulse, which could heat and explode the clusters near the laser focus before the main pulse arrives. We have purposely spoiled the pulse contrast
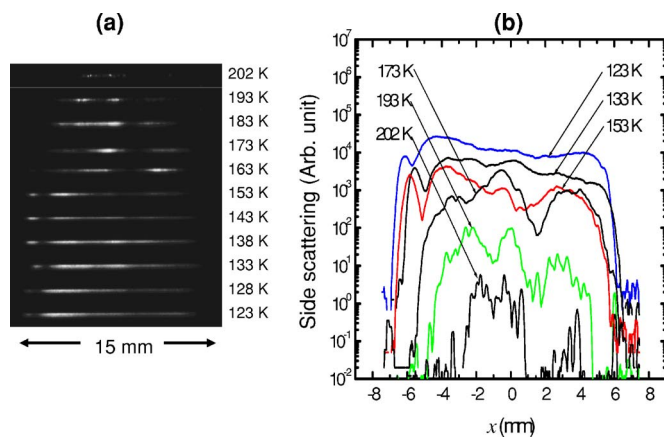
FIG. 12. (Color online) (a) N_2 cluster Rayleigh scattering images from an elongated jet, as a function of valve temperature and at a backing pressure of 400 psi. The weak 532 nm probe pulse propagates along the slot orifice, 2 mm above it. (b) Central lineouts of the scattering images in (a).

to promote this effect, and an x-ray emission dip occurs at a different axial location, as seen in the pinhole image in Fig. 11. Therefore prepulse is not a factor. We have previously characterized our elongated cryogenic jet with a technique combining Rayleigh scattering and interferometry measurements [12] and have found that axial uniformity of cluster flows of argon and nitrogen improves with valve cooling. The side scattering yield from a weak, axially propagating probe pulse is shown in Fig. 12 as a function of valve temperature. At $T = 173$ K it is seen that the scattering profile has a dip, with further nonuniformity appearing at even higher temperatures. Thus the double humped x-ray emission is likely an artifact of the cluster flow profile along the nozzle slot orifice.

V. CONCLUSIONS

We have shown that by using elongated clustered gas jets, extended laser self-guided propagation can produce strongly heated, high aspect ratio plasmas. The guiding process is limited either by the length of the cluster jet or by the absorption in the cluster plasma. We have diagnosed the extended plasmas with x-ray spectroscopy and x-ray pinhole imaging, and these images are consistent with optical interferometric, shadowgraphic, and scattering images. Strong broadening to the blue of the Ly-α line of OVIII and the He-β line of OVII, and a truncation of the red wings is well explained by emission from high energy ions moving toward the spectrometer and absorption of emission from ions moving away from the spectrometer. Simulations suggest that the measured emission is driven by electron collisions at early times in the laser-cluster interaction followed by the cascade emission fed by a three-body recombination at times after the laser pulse.

[1] E. Esarey, P. Sprangle, J. Krall, and A. Ting, IEEE Trans. Plasma Sci. **24**, 252 (1996).

[2] E. Seres, J. Seres, F. Krausz, and C. Spielmann, Phys. Rev. Lett. **92**, 163002 (2004); H. M. Milchberg, C. G. Durfee, III, and T. J. McIlrath, *ibid.* **75**, 2494 (1995); A. Rundquist *et al.*, Science **280**, 1412 (1998).

[3] M. Tabak *et al.*, Phys. Plasmas **1**, 1626 (1994).

[4] See, for example, C. E. Clayton, K. C. Tzeng, D. Gordon, P. Muggli, W. B. Mori, C. Joshi, V. Malka, Z. Najmudin, A. Modena, and A. E. Dangor, Phys. Rev. Lett. **81**, 100 (1998); K. Krushelnick, A. Ting, C. I. Moore, H. R. Burris, E. Esarey, P. Sprangle, M. Baine, *ibid.* **78**, 4047 (1997); J. Fuchs *et al.*, *ibid.* **80**, 1658 (1998); A. B. Borisov *et al.*, *ibid.* **68**, 2309 (1992).

[5] P. Sprangle, E. Esarey, J. Krall, and G. Joyce, Phys. Rev. Lett. **69**, 2200 (1992); T. M. Antonsen and P. Mora, *ibid.* **69**, 2204 (1992); P. Chessa, E. Dewispelaere, F. Dorchies, V. Malka, J. R. Marques, G. Hamoniaux, P. Mora, and F. Amiranoff, *ibid.* **82**, 552 (1999).

[6] A. B. Borisov, A. McPherson, K. Boyer, and C. K. Rhodes, J. Phys. B **29**, L113 (1996).

[7] H. M. Milchberg, S. J. McNaught, and E. Parra, Phys. Rev. E **64**, 056402 (2001).

[8] K. Y. Kim, I. Alexeev, E. Parra, and H. M. Milchberg, Phys.

Rev. Lett. **90**, 023401 (2003).

[9] I. Alexeev, T. M. Antonsen, K. Y. Kim, and H. M. Milchberg, Phys. Rev. Lett. **90**, 103402 (2003).

[10] T. Taguchi, T. M. Antonsen, Jr., and H. M. Milchberg, Phys. Rev. Lett. **92**, 205003 (2004).

[11] E. Parra, I. Alexeev, J. Fan, K. Kim, S. J. NcNaught, and H. M. Milchberg, Phys. Rev. E **62**, R5931 (2000).

[12] K. Y. Kim, V. Kumarappan, and H. M. Milchberg, Appl. Phys. Lett. **83**, 3210 (2003).

[13] O. F. Hagena and W. Obert, J. Chem. Phys. **56**, 1793 (1972); J. Wormer *et al.*, Chem. Phys. Lett. **159**, 321 (1989); J. Farges *et al.*, Chem. Phys. **84**, 3491 (1986).

[14] A. Ya. Faenov *et al.*, Phys. Scr. **50**, 333 (1994); I. Yu. Skobelev *et al.*, JETP **81**, 692 (1995).

[15] C. Jungreuthmayer, M. Geissler, J. Zhanghellini, and T. Brabec, Phys. Rev. Lett. **92**, 133401 (2004); G. M. Petrov, J. Davis, A. L. Velikovich, P. Kepple, A. Dasgupta, R. W. Clark, A. B. Borisov, K. Beyer, and C. K. Rhodes, Phys. Rev. E **71**, 036411 (2005).

[16] G. N. Gibson, R. R. Feeman, and T. J. McIlrath, Phys. Rev. Lett. **67**, 1230 (1991).

[17] C. Stenz *et al.*, Quantum Electron. **30**, 721 (2000); A. I. Magunov *et al.*, Laser Part. Beams **21**, 73 (2003).

[18] S. Dobosz *et al.*, JETP **88**, 1122 (1999).

[19] I. I. Sobelman, *Atomic Spectra and Radiative Transitions* (Springer-Verlag, Berlin, 1979).

[20] A. Yariv, *Quantum Electronics*, 2nd ed. (Wiley, New York, 1975).

[21] NIST elemental data index (http://physics.nist.gov/ PhysRefData/Elements)

[22] H. R. Griem, *Spectral Line Broadening by Plasma* (Academic Press, New York, 1974).